

Enhancing the electronic and optical performance of dye-sensitized solar cells with alizarin-based dyes: DFT/TDDFT investigations

Rajaa Diany^{a,b}, Said Kerraj^c, Mohamed Kadour Atouailaa^{d,e}, Ahmed Arif^{d,e}, Abdelkhalk Aboulouard^{f,g,h,*}, Mustapha Boulghalat^e, Abdessamad Tounsi^a, Mohammed Salah^b and Mohammed El idrissi^{d*}

^aFaculty of Science and Techniques, Sultan Moulay Slimane University, Beni Mellal, Morocco

^bFaculty of Sciences, Chouaib Doukkali University, El Jadida, Morocco

^cFaculty of Sciences Ben M'Sik, University Hassan II, Casablanca, Morocco

^dTCPA, Faculty Polydisciplinary Sultan Moulay Slimane University, Beni-Mellal, Morocco

^eLC2MCFaculty of Sciences and Technologies, Sultan Moulay Slimane University, Beni-Mellal, Morocco

^fResearch Laboratory in Physics and Engineering Sciences, Polydisciplinary Faculty, Beni-Mellal, Morocco

^gScience and Engineering Lab for Energy, National School of Applied Sciences, El Jadida, Morocco

^hHigher School of Education and Training, Beni-Mellal, Morocco

CHRONICLE

Article history:

Received October 3, 2024

Received in revised form

November 4, 2024

Accepted February 19, 2025

Available online

February 19, 2025

Keywords:

Alizarin-based dyes

Dye-sensitized solar cells

DFT

TD-DFT

Photovoltaic materials

Optical properties

Electronic properties

ABSTRACT

Dye-sensitized solar cells (DSSCs) offer several advantages over traditional silicon-based solar cells, such as lower cost, versatility, and transparency. Titanium dioxide (TiO₂) is widely used as a photocatalyst in DSSCs due to its chemical stability, high photocatalytic activity, photostability, and non-toxicity. This study provides a computational analysis of the geometric, electronic, optical, and photovoltaic properties of ten novel dyes using Density Functional Theory (DFT) and Time-Dependent DFT (TD-DFT). To our knowledge, these dyes have not been previously explored in the literature. Our findings indicate that structural modifications can significantly enhance the electronic, optical, and photovoltaic properties of these dyes. The B3LYP functional was identified as the most effective for predicting the geometric and electronic properties, while TD-DFT calculations with the CAM-B3LYP functional and the 6-31G(d,p) basis set accurately predicted the absorption properties. The absorption maxima of the dyes ranged from 427.82 nm to 755.93 nm, with strong UV-Vis absorption attributed to delocalized π - π^* transitions. The calculated band gaps varied from 1.928 eV to 2.425 eV, showing that increased conjugation leads to reduced band gaps and improved dye performance. Open-circuit voltage (V_{oc}) values for TiO₂ ranged from 0.893 eV to 1.38 eV, suggesting good potential for efficient electron injection into the TiO₂ conduction band. In conclusion, the ten novel dyes studied exhibit significant potential for use in DSSCs, and the theoretical methods employed here offer a reliable framework for predicting the properties of other materials. This approach can guide the development of new materials designed to improve the performance of DSSCs.

© 2025 by the authors; licensee Growing Science, Canada.

1. Introduction

Dye-sensitized solar cells (DSSCs) are type of photovoltaic solar cells that are considered as a third-generation which efficiently converts sunlight into electrical power. They are particularly promising due to their low cost, ease of fabrication, and impressive efficiency in harnessing solar energy¹⁻³.

DSSCs were first developed by Grätzel and O'Regan in 1991, marking a significant leap forward in the field of photovoltaic technology. Since then, these cells have been the focus of extensive research and development, further improving their performance and application potential. Structurally, DSSCs are composed of several key components, including a transparent conductive substrate, an electrolyte, a counter electrode, and a photoanode⁴⁻⁷. The photoanode, which is crucial to the cell's function, consists of a layer with a porous nanoparticles coated with a light-sensitive dye. The photons

* Corresponding author

E-mail address m.elidrissi2018@gmail.com (A. Aboulouard) a.aboulouard@usms.ma (M. El idrissi)

of sunlight are captured by the dye and resulting in the generation of electron-hole pairs, which are essential for the cell's operation⁸⁻¹⁰.

In DSSCs, the movement of charge carriers is crucial for the conversion of sunlight into electrical power^{11,12}. Holes generated in the photoanode move toward the electrolyte, while electrons are directed to the transparent conductive substrate¹³⁻¹⁵. The electrolyte plays a key role as a redox mediator, facilitating the transfer of electrons to the counter electrode and recharging the dye^{16,17}. The process is completed when electrons and holes recombine at the counter electrode, closing the electrical circuit. The performance of DSSCs is influenced by many factors, such as the characteristics of the dye used, the structure of the photoanode, and the composition of the electrolyte. In this context, inorganic or organic metal complex dyes are favored due to their tunable electrical properties and good coefficients of absorptions^{18,19}. Additionally, semiconductors like tin oxide (SnO₂), zinc oxide (ZnO), and TiO₂ are particularly suitable for constructing flexible and efficient photoanodes^{20,21}.

DSSCs present several features over traditional silicon solar cells, including cost-effectiveness, versatility, and transparency²²⁻²⁵. Titanium dioxide (TiO₂) is commonly employed as a photocatalyst in DSSCs, especially in initiatives aimed at mitigating freshwater shortages^{26,27}, due to its chemical durability, high photocatalytic activity, photostability, and non-toxicity²⁸⁻³⁰. However, anatase TiO₂ has inherent drawbacks, such as low activity and a wide band gap of 3.2 eV, which limits its sensitivity to visible light and reduces its solar energy absorption efficiency^{31,32}. Recent advancements in DSSC technology have addressed some of these challenges by developing a new photoanode composite that includes hollow TiO₂ spheres for improved light scattering, gold nanoparticles with significant surface plasmon resonance effects, and up-conversion nanoparticles capable of converting near-infrared photons into visible photons. These innovations highlight the significant potential of DSSCs to revolutionize the photovoltaic industry by offering an efficient means of converting solar energy into electrical power. Nevertheless, more development and research are required to enhance the efficiency, durability, and lifespan of these systems, ensuring they can meet future energy demands³³⁻²⁶.

Optimizing the efficiency of DSSCs heavily relies on the careful selection of light-sensitive dye molecules and nanocrystalline materials for the photoanode electrodes. An effective strategy for enhancing DSSC efficiency involves using donor-acceptor molecules, which consist of an acceptor component, such as carboxylate, and a donor component, such as amine. Hybrid alizarin-based dyes, which combine an acceptor moiety (alizarin) with an electron-donating moiety (carbazole), exemplify this approach. These dyes leverage the charge transfer of photo-induced features of the donors organic dye, which are crucial for the enhancement of efficient DSSCs. A thorough analysis of the optical absorption characteristics of ten alizarin-based dyes has been performed, with their molecular structures depicted in **Fig. 1**.

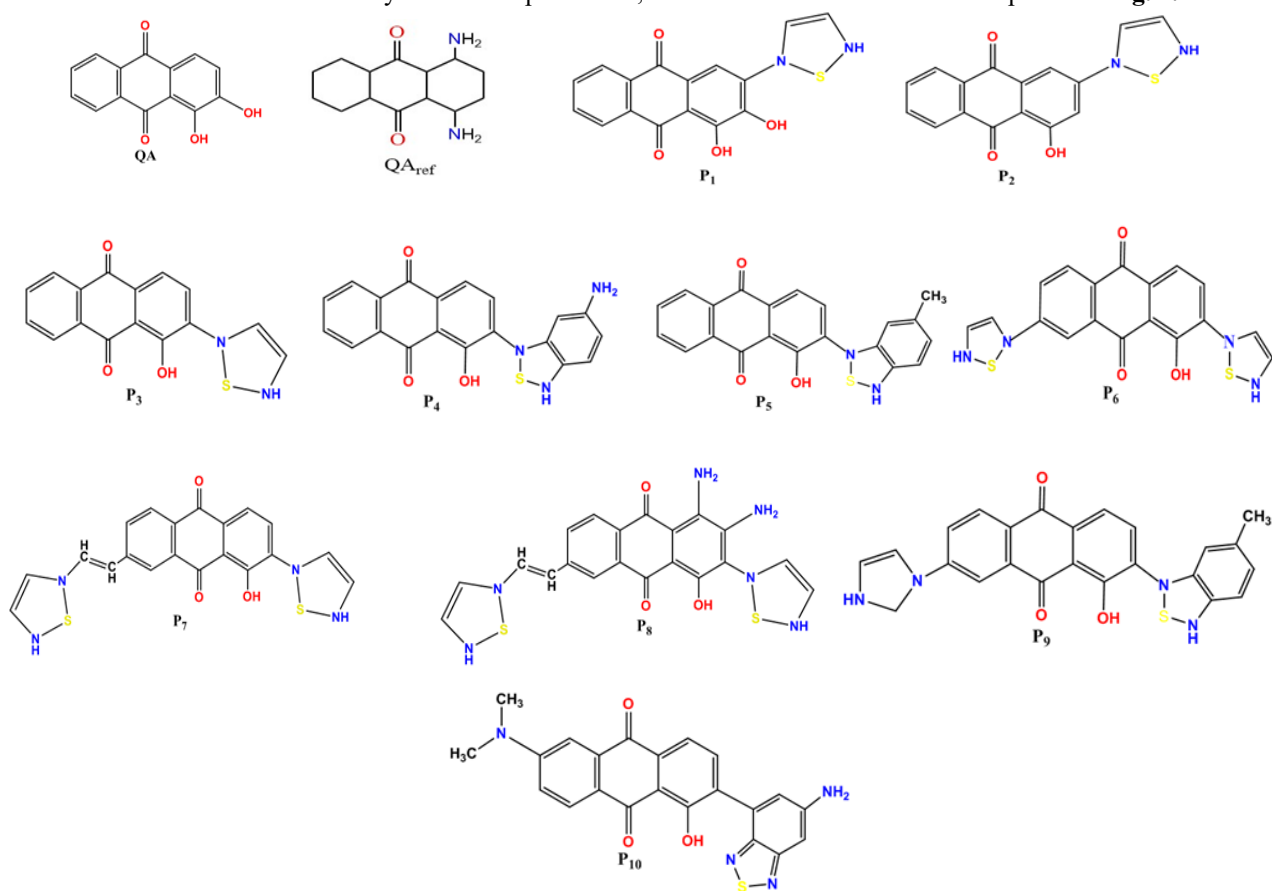


Fig. 1. Dye structures QA, QA_{ref} and P_i (i=1-10)]

In applications such as solar cells, the transfer of intramolecular charge—referring to the internal electron's movement in a molecule as they shift between different electronic states—is crucial. A key characteristic in this context is the energy gap, or band gap, which determines a material's capability to absorb photons and generate the photocurrent. The gap energy is the difference in energy between the lowest unoccupied molecular orbital (LUMO) and the highest occupied molecular orbital (HOMO). A narrow band gap facilitates the creation of charge carriers (holes and electrons) as it indicates that the energy required for an electron to transition from the low-level HOMO to the high-level LUMO is relatively low.

For solar cell applications, organic compounds with elevated HOMO levels and reduced LUMO levels are highly effective³⁷. The efficiency of these substances in photovoltaic cells and other optoelectronic systems is strongly impacted by an optimal structural configuration, effective internal charge migration, and a suitable energy gap. Understanding the geometric and electronic properties of organic dyes in both their neutral and excited states requires the application of theoretical methods like Density Functional Theory (DFT) and Time-Dependent Density Functional Theory (TD-DFT)^{38,29}.

2. Theoretical study of alizarin-based solar cells

Modeling a molecule generally starts with generating a visual representation of its molecular geometry or atomic arrangement. Subsequently, a theoretical framework, such as quantum mechanics or molecular dynamics, is employed to refine the electronic structure and assess the molecule's physical properties. In this paper, DFT was chosen as the modeling method. The calculations were conducted using the Gaussian 09 software on our personal computers.

2.1 Calculation function selection

The electronic characteristics of new chromophores investigated by quantum computing, such as the energy levels of their frontier orbitals (HOMO and LUMO) and the gap energy, need experimental validation. As shown in **Fig. 2**, this procedure allowed us to compare such properties that were derived theoretically and experimentally. In the alizarin (AQ) family, anthraquinone (AQ_{ref}) is utilized as a reference molecule (**Fig. 1**).

A comparison of the energy gap, HOMO, and LUMO values determined experimentally with those obtained using various quantum computing techniques (B3LYP, WB97XD, B3PW91, PBEPBE, BPV89, and CAM-B3LYP)⁴⁰ is shown in **Fig. 2**. This comparison method is commonly used in the literature to determine the most suitable functional for a given study⁴¹⁻⁴³.

The findings demonstrate that B3LYP produces results that closely resemble the experimental data when used with the 6-31G(d,p) basis set⁴⁴⁻⁴⁷. Therefore, we selected the B3LYP functional, as it provided the closest energy gap, HOMO, and LUMO values to the experimental result.

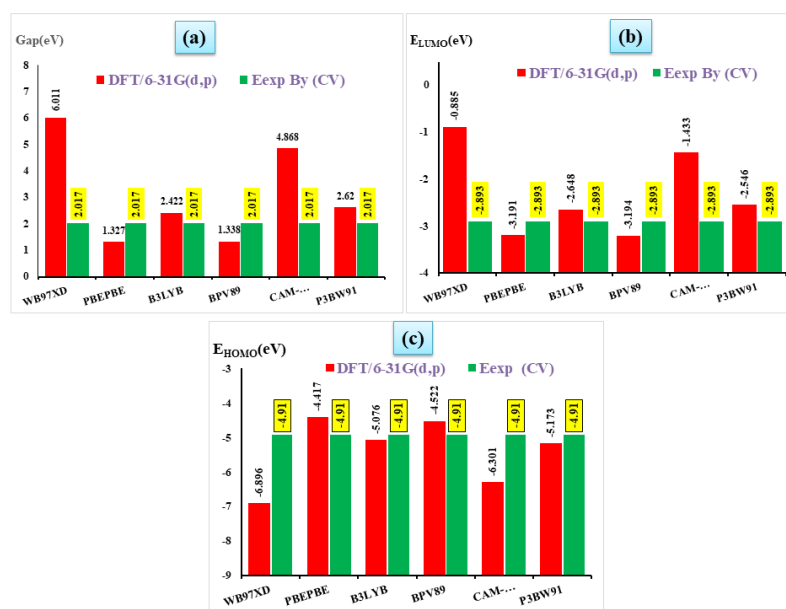


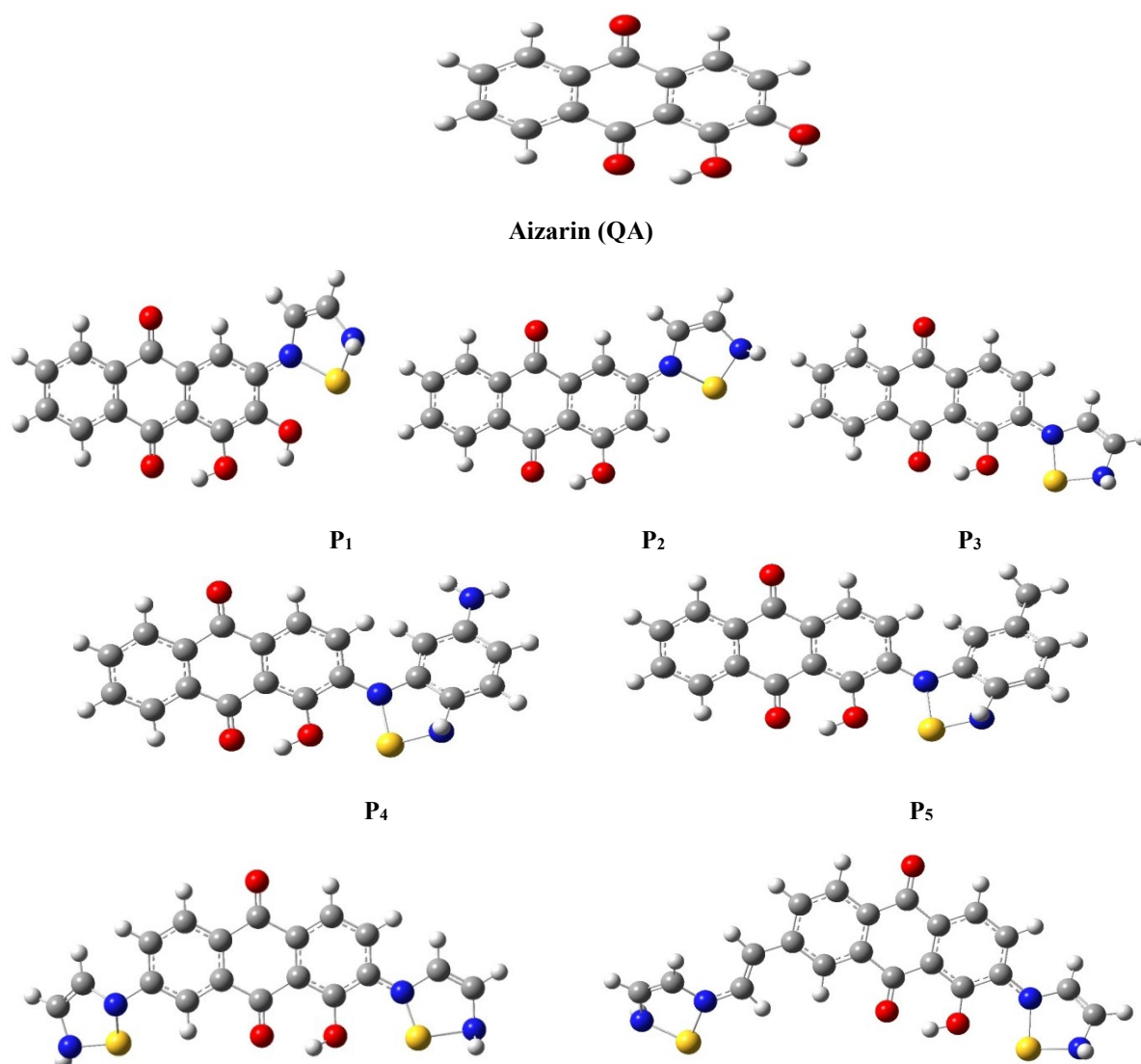
Fig. 2. Comparison of energy gap (a), LUMO molecular orbital energy (b) and HOMO molecular orbital energy (c) simulated by different quantum methods and experimental (CV: Cyclic Voltammetry data).

Based on measurements of the energy gap, the LUMO and HOMO molecular orbital of the reference dye, we remark that the B3LYP function in the 6-31G(d, p) base is in agreement with experimental values⁴⁸. After determining the most appropriate function, the designed dyes are optimized by TD-DFT computations. In particular, the TD-DFT-B3LYP method

is used to examine the optical, electronic, and photovoltaic proprieties with the 6-31G(d,p) basis set. The lack of imaginary frequencies in all dyes signifies that the optimized geometries have an overall minimum (Table S1).

2.2 Calculation Procedure and Geometric Structure of Dyes

First, the optimization procedure was applied to identify the stable conformation of the dyes. Several structures were optimized using the 6-31G (d,p) basis set, which was found to be the most reliable for our system^{48,49}. Concurrently, we performed similar calculations using Becke's B3 three-parameter hybrid function combined with non-local Lee-Yang-Parr (LYP) correlation, generally referred to as the B3LYP method. The same 6-31G (d,p) basis set was utilized for this approach. Subsequently, the B3LYP-optimized geometries for the Pi dyes ($i = 1-10$) were analyzed using TD-DFT with the CAM-B3LYP functional and the 6-31G (d,p) basis set to determine ground-state energies, excited-state energies, and oscillator strengths⁴³. This analysis provided insights into the HOMO and LUMO levels, the HOMO-LUMO gap, and the absorption maximum (λ_{\max}). The most stable conformations were obtained after optimization in both ground and excited states using the DFT method with the B3LYP functional and the 6-31G (d,p) basis set. The molecular structures of the optimized dyes (QA and Pi, with $i = 1-10$) are presented in **Fig. 3**, which explains more clearly the structural changes made and illustrates in greater detail the molecular configurations obtained after the optimization procedure was completed.



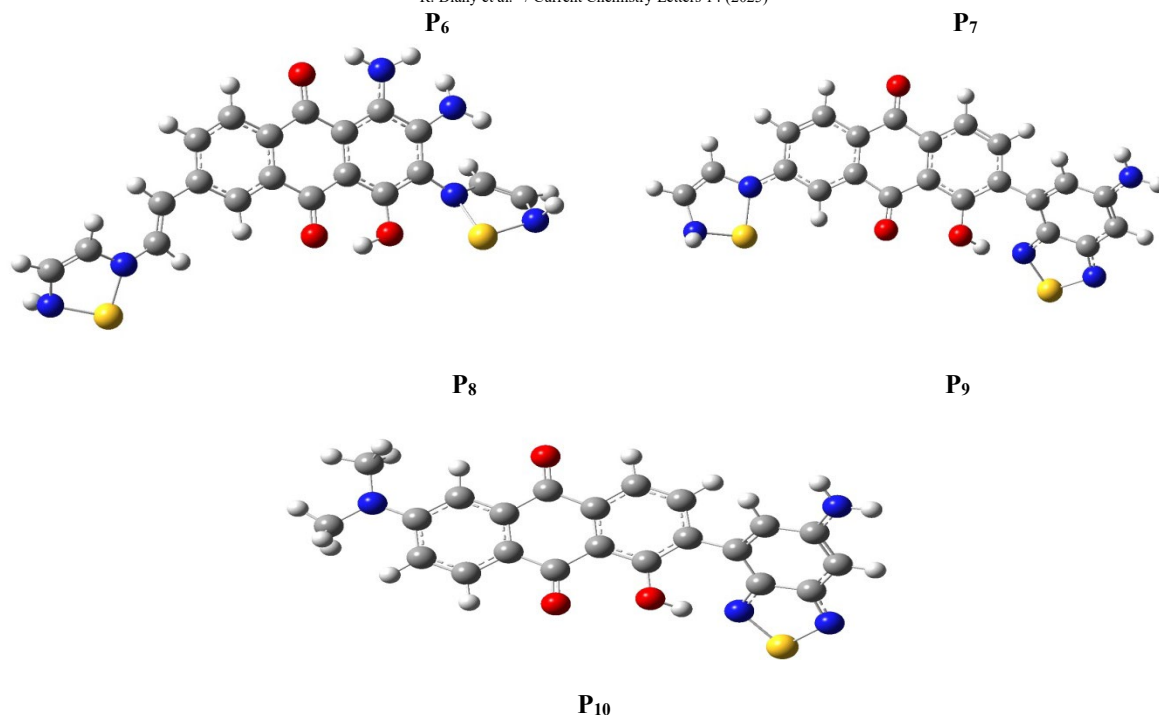


Fig. 3. The optimized structures of dyes (QA, and P_i with $i = 1-10$) obtained using B3LYP/6-31G(d,p) level

2.3 Computational details

Understanding the HOMO and LUMO orbitals is essential to comprehending how all chemical compounds behave physicochemically. In this context, the DFT/B3LYP/6-31G(d,p) method was employed to optimize the structures of these molecules. To investigate the electronic characteristics of compounds, the energy gap (E_g) was calculated. As is well knowledge, the energy gap has the following definition and can be connected to certain molecular characteristics like electrical conductivity and kinetic stability (reactivity)⁵⁰.

$$E_g = E_{LUMO} - E_{HOMO} \quad (1)$$

E_{LUMO} and E_{HOMO} represent the LUMO energy level and the HOMO energy level, respectively. Employing the DFT/B3LYP/6-31G(d,p) approach on the optimized structures, we calculated several chemical properties, including electronegativity (χ), electronic chemical potential (μ), overall hardness (η), and overall softness (S). Zhou et al. notes that electronegativity is represented as the negative of the Lagrange multiplier, which corresponds to the electronic chemical potential⁵¹.

$$\mu = \left(\frac{\partial E}{\partial N} \right)_V = -\chi \quad (2)$$

where E represents the electronic energy, N the number of electrons and V corresponds to the potential generated by the nuclei. The electronic chemical potential μ and the global hardness η are calculated from the energies of the boundary molecular orbital's E_{HOMO} and E_{LUMO} as follows^{51,52}.

$$\mu = (E_{HOMO} + E_{LUMO})/2 \quad (3)$$

$$\eta = (E_{LUMO} - E_{HOMO})/2 \quad (4)$$

The system's sensitivity to perturbations is quantified by softness (S) and electrophilicity power (ω), which are related to changes in electron density in response to variations in the external potential or electron count. Softness is the inverse of hardness (η) and is frequently used in density functional theory (DFT) calculations. It can be mathematically expressed as follows.

$$S = \frac{1}{2\eta} \quad (5)$$

$$\omega = \frac{\mu^2}{2\eta} \quad (6)$$

The density of short-circuit current (J_{sc}) in DSSCs is given by the Eq. (7)⁵³.

$$J_{sc} = \int \text{LHE}(\lambda) \Phi_{inj} \eta_{coll} d\lambda \quad (7)$$

where Φ_{inject} is the efficiency of electron injection, $\eta_{collect}$ the efficiency of charge collection, and $\text{LHE}(\lambda)$ is the light harvesting efficiency. To attain a high, short-circuit current (J_{sc}), the effective dyes utilized in the DSSCs necessitate a substantial light harvesting efficiency (LHE) as specified by Eq. (8)⁵⁴.

$$\text{LHE} = 1 - 10^{-f} \quad (8)$$

The dye's oscillator strength (f), especially when it comes to wavelength (λ_{max}), is unquestionably essential for effective light harvesting in dye-sensitized solar cells (DSSCs). An increased value of f signifies a more robust absorption of light, thereby augmenting the sensitizer's capacity to harvest light and ultimately enhancing the DSSC's overall efficiency. Moreover, the injection efficiency (Φ_{inject}) is a significant factor that also contributes to a high J_{sc} . A higher J_{sc} is the outcome of a larger Φ_{inject} . The injection driving force (ΔG_{inject}), which is defined in detail in reference⁵⁵, is related to this injection efficiency. Understanding and maximizing the performance of DSSCs requires an understanding of the fundamental relationship between Δ_{inj} and ΔG_{inject} .

$$\Delta G_{inject} = E_{dye}^* - E_{CB} \quad (9)$$

The notation E_{dye}^* represents the dye's excited state oxidation potential, whereas the notation E_{CB} represents the semiconductor TiO_2 's ground state reduction potential. Comprehending the transfer of electron mechanisms in DSSCs requires an understanding of these values. The value for E_{dye}^* was calculated using Eq.10 from reference⁵⁴, whereas the conduction band edge potential of TiO_2 (E_{CB}) used is 4.00 eV, as reported in reference^{56,57}.

$$E_{dye}^* = E_{dye} - E_{exp} \quad (10)$$

The formula $E_{dye} = -E_{HOMO}$ represents the potential oxidation of the dye's ground state. Moreover, the potential is determined by the absorption energy E_{exp} , which is associated with the maximum wavelength λ_{max} in the UV-visible and near-IR domains. In addition, equation 11 provides a basis for estimating open-circuit photovoltaic V_{oc} ^{58,59}.

$$V_{oc} = E_{LUMO} - E_{CB} \quad (11)$$

where E_{CB} denotes the band conduction of TiO_2 and E_{LUMO} denotes the energy level of the dye's LUMO⁶⁰.

2.4 Results and discussion

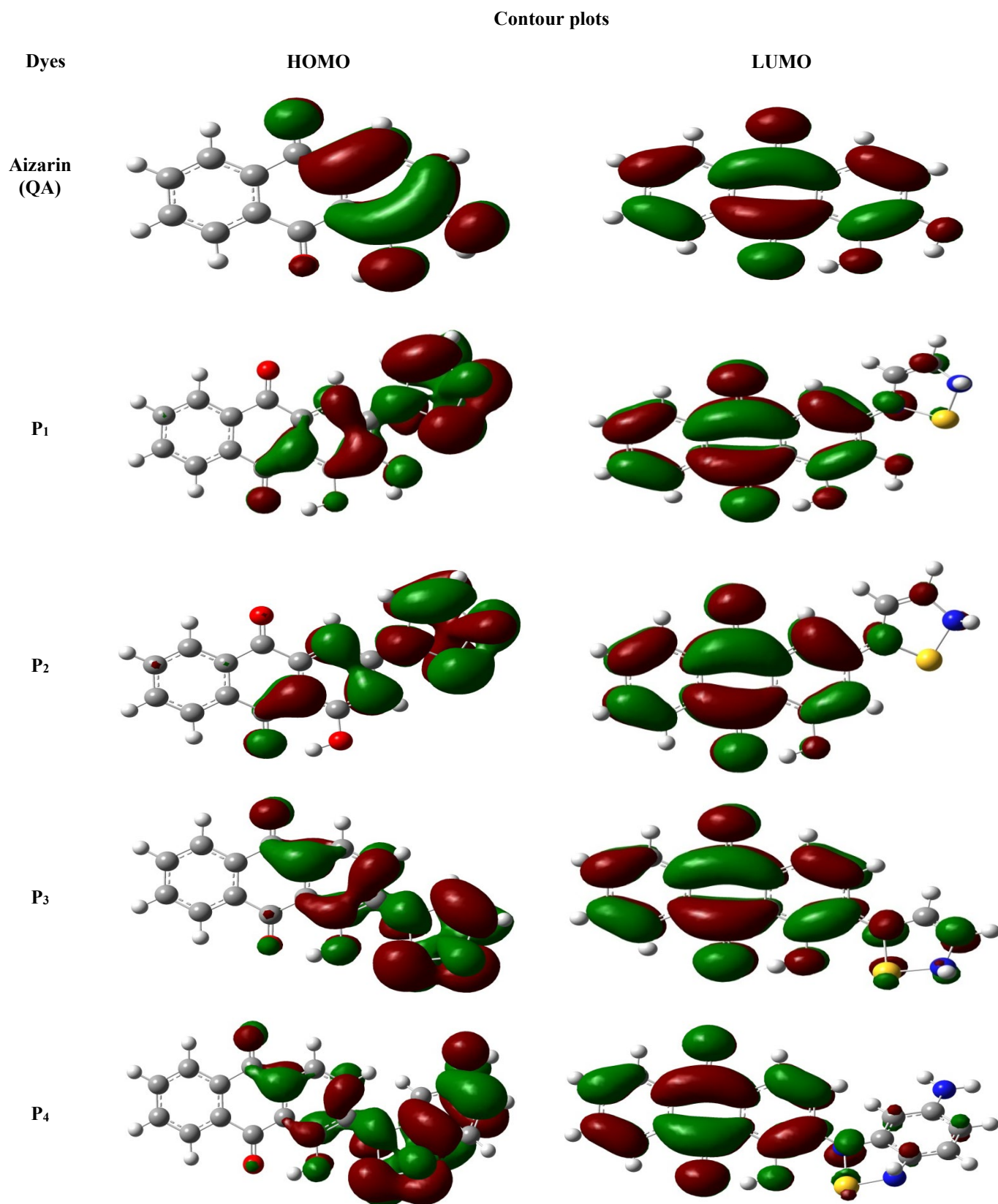
2.4.1 Frontier molecular orbital

The energy gap of a compound significantly influences its photocurrent. A smaller band gap facilitates the movement of electrons from the HOMO to the LUMO level upon absorbing light of a certain wavelength. Understanding the HOMO and LUMO orbital's is essential for grasping the physico-chemical properties of p-type the chemical compounds. Furthermore, based on the representation of the HOMO, the C=C bonds display a p-bonding nature and exhibit an antibonding phase concerning their adjacent C=C units. To delve into their importance, we utilized the DFT/B3LYP/6-31G(d,p) approach to optimize structures, displaying the HOMO and LUMO orbital's in **Fig. 4**. Based on this figure, we can see that for the HOMO level in the ground state, the density of electron is mainly located on the thiophene part linked to the hydroxide-bearing part of the anthraquinone (QA) of dyes P1-P8, with the exception of P9 and P10 where this density is located on the other part of QA, with a strong influence on the donor group. The HOMO orbitals of the nine dyes under study have a binding character to the bonds between the acceptor and donor groups. Regarding the LUMO level, the density of electron is primarily concentrated on the QA part (electron acceptor group) of the **P1-P8** dyes, suggesting a high abundance of electrons in this region (**Fig. 4**). However, in the case of dyes **P9** and **P10**, the density is specifically situated on the benzo[c] thiophene moiety that is connected to QA. The LUMO orbitals of the ten dyes explored exhibit an anti-bonding nature on the bonds connecting the acceptor and the donor group.

2.4.2 Dyes electronic properties

The calculations of Frontier Molecular Orbital (FMO) energies provide detailed insights into excited state transitions and absorption spectra in dyes. The E_{HOMO} and E_{LUMO} values of the dyes and TiO_2 have been determined and are shown in

Table 1. Furthermore, reactivity indices based on DFT calculations, such as η , S , μ , χ , and ω , are calculated to examine electronic characteristics (**Table 1**).



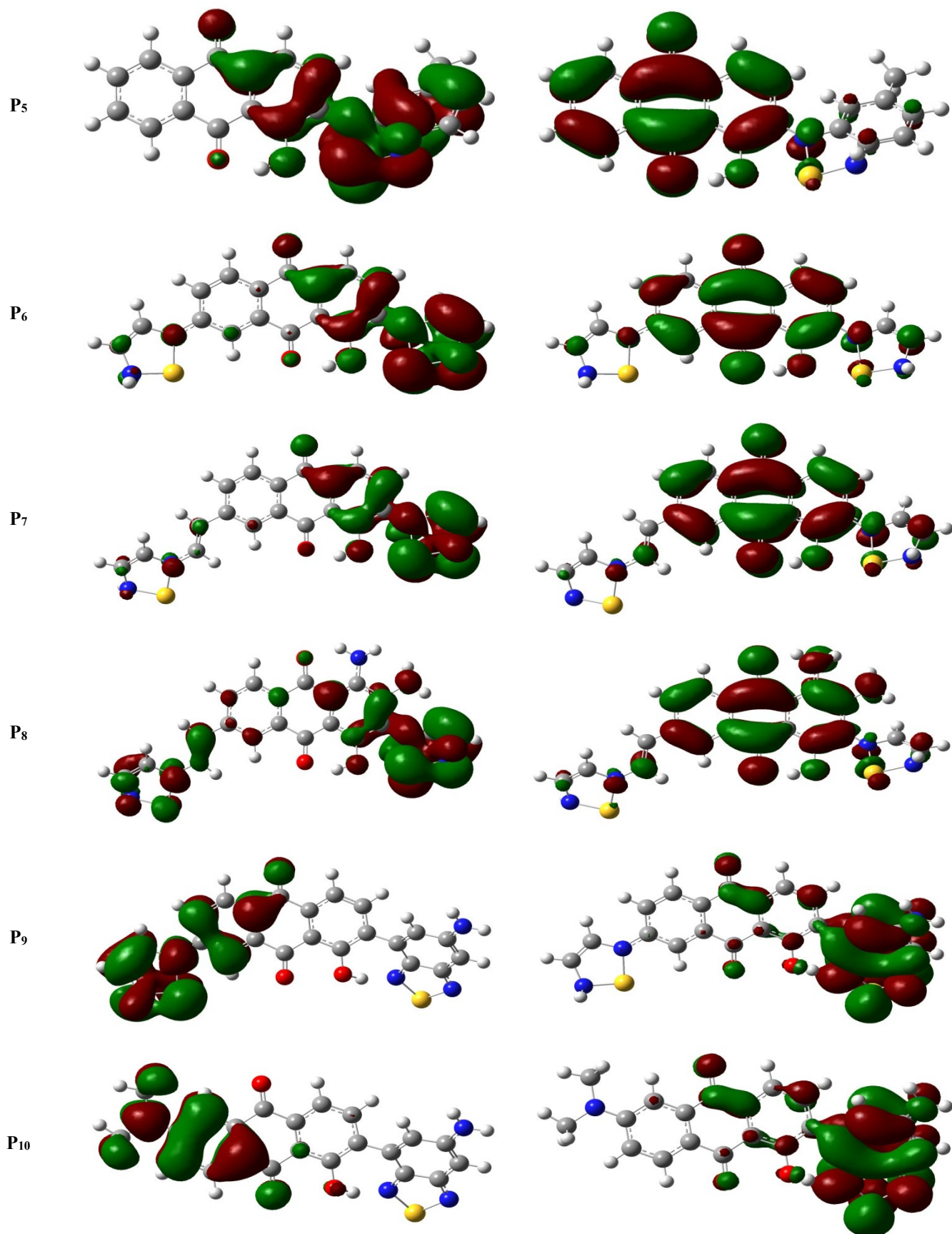


Fig. 4. The HOMO and LUMO orbital contours of the dyes studied, QA and Pi ($i=1-10$).

Table 1. E_{HOMO} , E_{LUMO} , E_g and DFT calculated reactivity indices (η , S , μ , χ and ω) of the dyes investigated in eV.

Dyes	E_{HOMO}	E_{LUMO}	E_g	η	S	μ	χ	ω
QA	-6.40	-3.22	3.18	1.59	0.31	-4.82	4.82	7.30
P ₁	-5.01	-3.04	1.97	0.99	0.51	-4.03	4.03	8.20
P ₂	-5.28	-2.99	2.30	1.15	0.43	-4.13	4.13	7.41
P ₃	-4.94	-3.01	1.93	0.96	0.52	-3.97	3.97	8.20
P ₄	-5.01	-3.04	1.97	0.98	0.51	-4.03	4.03	8.28
P ₅	-5.23	-3.11	2.12	1.06	0.47	-4.17	4.17	8.20
P ₆	-4.83	-2.88	1.95	0.97	0.51	-3.86	3.86	7.68
P ₇	-4.82	-2.85	1.97	0.98	0.50	-3.83	3.83	7.48
P ₈	-4.88	-2.62	2.26	1.13	0.44	-3.75	3.75	6.22
P ₉	-5.02	-3.00	2.02	1.01	0.49	-4.01	4.01	7.96
P ₁₀	-5.38	-2.96	2.42	1.21	0.41	-4.17	4.17	7.18
TiO ₂ (CB)	-7.16 ⁵⁴	-4.00 ⁵⁴	3.16	1.58	0.32	-5.58	5.58	9.85

The findings listed in **Table 1** indicate that TiO₂ compound exhibits the least chemical potential value μ (-5.58) in comparison to the other dyes. Electron transfer occurs from compounds with higher chemical potential to those with lower chemical potential. Given that the chemical potential of TiO₂ is smaller than that of the other P_i(i=1-10) compounds, we can deduce that TiO₂ serves as an electron acceptor, while the others function as electron donors.

According to the results in **Table 1**, and by comparing the differential electronegativity obtained. TiO₂ is identified as the molecule with the highest electronegativity (5.58) than the dyes P (χ = 3.75 to 4.17 eV), indicating a strong tendency to attract electrons. This attraction is expected to occur between TiO₂ as the acceptor and the other P_i molecules as donors. On the other hand, TiO₂ exhibits the highest hardness at 1.58 eV, indicating resistance to rearrangement in its electronic structure, resulting in lower reactivity. Following TiO₂, Compound P₁₀ ranks second with a hardness of 1.21, succeeded by P₂ at 1.15, and finally P₈ at 1.13 [$\eta(\text{CB}) > \eta(\text{P}_{10}) > \eta(\text{P}_2) > \eta(\text{P}_8)$], along with other compounds showing nearly identical hardness values. Compounds P₄, P₆, and P₃ are likely to undergo electronic structure changes via chemical reactions, potentially forming covalent bonds. The transfer of electronic flux from the dyes to the semiconductor is supported by the dyes' lower global hardness and higher softness compared to TiO₂, as seen in **Table 2**.

The gap value is a crucial measure for assessing the quality of compounds. To enhance the aromaticity of these compounds, the most efficient approach is to incorporate or connect electron donor groups and stabilize the nucleus and the acceptor group.

The calculations were performed using the DFT approach, specifically employing the B3LYP functional and the Pople base 6-31G (d,p) with high quality. The results in **Table 2** present the HOMO, LUMO, and gap energy of various optimized molecules obtained through B3LYP/6-31G (d,p). The data indicates that the energy gap increases from compound P₃ to compound P₁₀, likely due to an increase in the substituent's electron-donating ability in the molecule. The determined band gap of the examined molecules ranged from 2.425 to 1.928 eV, with the following ascending order of increases: P₁₀ > P₂ > P₈ > P₅ > P₉ > P₇ > P₁ > P₄ > P₆ > P₃. The data in Table 2 illustrates that dyes P₇, P₆, P₈ and P₃ [$E_{\text{HOMO}}(\text{P}_7) > E_{\text{HOMO}}(\text{P}_6) > E_{\text{HOMO}}(\text{P}_8) > E_{\text{HOMO}}(\text{P}_3)$] exhibit the highest HOMO energies when compared to other molecules. Consequently, these dyes are characterised by a soft character. CB stands out for having the lowest E_{HOMO} value, suggesting that it is more difficult compared to the other dyes. On the other hand, the ten dyes (P₁-P₁₀) have a high-energy LUMO around -3.00 eV while the semiconductor CB has a LUMO energy close to -4.00 eV. CB therefore has the characteristics of electrophilic species compared to the other compounds dyes studied, confirming its acceptor nature.

The E_{LUMO} and the E_{HOMO} values for the ten compounds studied have been identified, along with the E_{LUMO} and the E_{HOMO} of CB (TiO₂), as detailed in Table 1. According to the theory of frontier orbitals, when two molecules interact, the crucial frontier orbitals are the HOMO of one molecule and the LUMO of the other. This selection is made with the objective of minimising E_g between the two molecules. Figure 5 shows the possible interactions between the P₃ molecule and the CB compound.

Table 2. E_{HOMO} , E_{LUMO} , the $\text{LUMO}_{\text{CB}} - \text{HOMO}_{\text{P}_i}$ gap and the $\text{gap}_{\text{LUMO}_{\text{P}_i} - \text{HOMO}_{\text{CB}}}$ in eV.

Dyes	$E_{\text{HOMO}}(\text{eV})$	$E_{\text{LUMO}}(\text{eV})$	$\text{LUMO}_{\text{CB}} - \text{HOMO}_{\text{P}_i}$	$\text{gap}_{\text{LUMO}_{\text{P}_i} - \text{HOMO}_{\text{CB}}}$
P ₁	-5.01	-3.04	1.01	4.12
P ₂	-5.28	-2.98	1.28	4.18
P ₃	-4.94	-3.01	1.94	4.15
P ₄	-5.01	-3.04	1.01	4.11
P ₅	-5.23	-3.11	1.23	4.05
P ₆	-4.83	-2.88	1.83	4.27
P ₇	-4.82	-2.84	1.82	4.31
P ₈	-4.88	-2.62	1.88	4.54
P ₉	-5.02	-3.00	1.02	4.15
P ₁₀	-5.38	-2.96	1.38	4.2
TiO ₂	-7.16	-4.00	***	***

Table 2 illustrates the most favorable interaction effect between the electron donor group and the electron acceptor group on the compounds character and overall properties. The Calculations of the HOMO-LUMO gaps between the dyes and the conduction band (CB) of TiO₂ show that the most favorable interactions are those that between the **Pi** dyes as electron donors and the CB as electron acceptors because these interactions have a lower energy gap than that of the interaction between CB as electron donor and the dye as an electron acceptor. **Table 2** demonstrates that the energy differences between the HOMO of the electron donors (**P1-P10**) and the LUMO of the electron acceptor (CB) are greater than 0 eV. This suggests that there will be electrons transfer from the donor molecule (Pi) to the acceptor molecule TiO₂ (CB). To assess the potential for transfer of electron from the investigated excited molecules to the TiO₂ (CB), we conducted a comparison of the HOMO and LUMO levels (**Fig. 5**). Significantly, the dyes' LUMO values surpass the CB of TiO₂ (-4.0 eV). Moreover, the HOMO energy levels of all the dyes surpass the conduction band edge of TiO₂, suggesting that the transfer of photo-excited electrons from the dyes to TiO₂ could be highly effective for application in photovoltaic cells. The findings indicate that the assessed compounds exhibited lower electrophilic values (ω) compared to TiO₂ (9.96), suggesting their proficiency as electron donors. Consequently, the examined compounds demonstrate efficacy as electron donors in DSSCs devices, while TiO₂ excels as an electron acceptor.

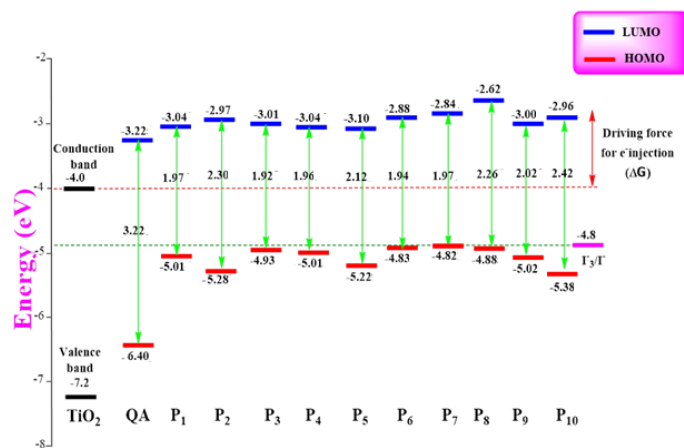


Fig. 5. Plot of HOMO and LUMO level energies for the dyes investigated, calculated using the B3LYP/6-31G(d,p) function.

2.4.3 Optical properties

In order to investigate the optical properties and electronic transitions of the dyes being analyzed, TD-DFT computations were conducted using the B3LYP functional and a 6-31G (d,p) basis set. The data obtained, as shown in **Table 3**, comprises the computed transition energies of (Pi) for absorption wavelength (λ_{abs}), vertical excitation energy (E_{ex}), oscillator strength (f), and the type of the transitions shown by these dyes. The least singlet electronic excitation is categorized as a standard $\pi-\pi^*$ transition.

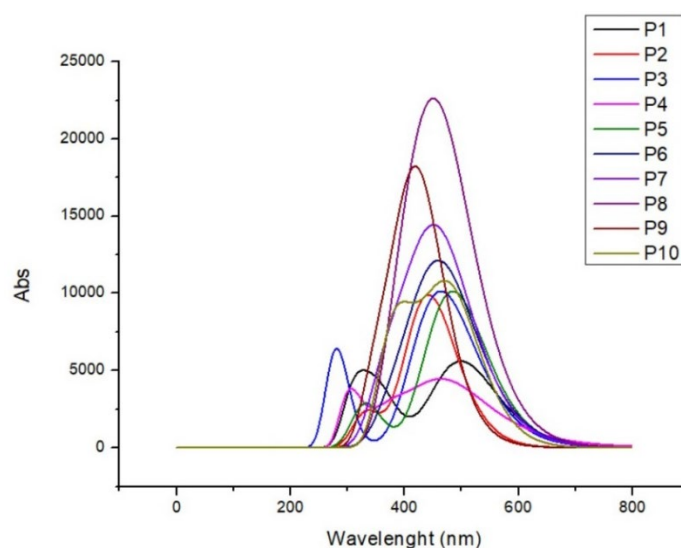


Fig. 6. Simulated UV-visible absorption spectra of the studied dyes, from data calculated using the TD-DFT method at the B3LYP/6-31G(d,p).

The absorption spectra of the ten dyes under study are simulated and given in **Fig. 6**. The spectra ranging from 200 to 800 nm indicates that the most intense absorption in the UV-visible region ($\lambda_{\text{max}} > 400$ nm) is associated with the HOMO-LUMO electronic transition for compounds **P**₁ to **P**₇. In contrast, for the other molecules: **P**₈ corresponds to HOMO-2→LUMO electronic transitions, **P**₉ to HOMO-1→LUMO transitions, and **P**₁₀ to HOMO-1→LUMO transitions, considering only the transitions with the highest oscillator strengths. Significantly, the absorption peaks move approximately 300 nm closer to the longer-wavelength, red region of the spectrum. The λ_{max} values for the ten dyes are ranked as follows: **P**₄ > **P**₆ > **P**₃ > **P**₇ > **P**₁ > **P**₈ > **P**₂ > **P**₉ > **P**₅ > **P**₁₀ (see **Table 3**). This bathochromic shift is attributed to the increasing conjugation within the compounds, particularly from **P**₁₀ to **P**₄. Specifically, the λ_{max} values are 427.82 nm for **P**₁₀, 484.63 nm for **P**₅, 490.34 nm for **P**₉, 490.64 nm for **P**₂, 499.38 nm for **P**₈, 500.85 nm for **P**₁, 520.27 nm for **P**₇, 523.70 nm for **P**₃, 526.77 nm for **P**₆, and 755.93 nm for **P**₄. Hence, comprehending the electronic and absorption properties of these molecules necessitates a thorough grasp of the significance of aromaticity and conjugation.

Table 3. Absorption spectra calculated using the TD-DFT method for the dyes investigated, based on their geometries optimized with the B3LYP/6-31G(d,p) level.

Dyes	Electronic Transition	λ_{abs} (nm)	E_{ex} (eV)	f	Transition caractère (%)
P ₁	S ₀ →S ₁	500.85	2.47	1.32×10 ⁻¹	HOMO→LUMO (63)
	S ₀ →S ₂	465.08	2.66	7.5×10 ⁻³	HOMO→LUMO+2 (54)
	S ₀ →S ₃	382.40	3.24	4.01×10 ⁻⁴	HOMO-5→LUMO (58)
	S ₀ →S ₄	358.80	3.45	8.21×10 ⁻²	HOMO-1→LUMO (64)
	S ₀ →S ₅	334.10	3.71	1.00×10 ⁻⁴	HOMO-7→LUMO (63)
	S ₀ →S ₆	313.78	3.95	9.77×10 ⁻²	HOMO→LUMO+5 (50)
P ₂	S ₀ →S ₁	490.64	2.53	1.30×10 ⁻³	HOMO→LUMO+1 (58)
	S ₀ →S ₂	442.15	2.80	2.43×10 ⁻¹	HOMO→LUMO (66)
	S ₀ →S ₃	383.00	3.24	1.00×10 ⁻¹	HOMO-4→LUMO (57)
	S ₀ →S ₄	338.00	3.67	2.10×10 ⁻³	HOMO-4→LUMO (31)
	S ₀ →S ₅	337.46	3.67	4.35×10 ⁻²	HOMO→LUMO+4 (65)
	S ₀ →S ₆	323.81	3.83	1.43×10 ⁻²	HOMO-1→LUMO (65)
P ₃	S ₀ →S ₁	523.70	2.36	2.42×10 ⁻¹	HOMO→LUMO (66)
	S ₀ →S ₂	469.78	2.64	1.27×10 ⁻²	HOMO→LUMO+2 (59)
	S ₀ →S ₃	388.22	3.19	1.00×10 ⁻⁴	HOMO-3→LUMO (64)
	S ₀ →S ₄	338.28	3.66	1.50×10 ⁻²	HOMO-7→LUMO (37)
	S ₀ →S ₅	337.16	3.68	8.00×10 ⁻⁴	HOMO-7→LUMO(52)
	S ₀ →S ₆	316.16	3.92	1.57×10 ⁻¹	HOMO→LUMO+5 (40)
P ₄	S ₀ →S ₁	755.93	1.64	1.01×10 ⁻¹	HOMO→LUMO(70)
	S ₀ →S ₂	560.70	2.21	6.21×10 ⁻²	HOMO-1→LUMO(70)
	S ₀ →S ₃	455.78	2.72	1.87×10 ⁻³	HOMO→LUMO+1(48)
	S ₀ →S ₄	446.61	2.77	5.00×10 ⁻⁴	HOMO-4→LUMO(68)
	S ₀ →S ₅	412.70	3.01	2.15×10 ⁻²	HOMO-1→LUMO(67)
	S ₀ →S ₆	404.04	3.07	6.17×10 ⁻²	HOMO→LUMO+1 (47)
P ₅	S ₀ →S ₁	484.63	2.56	2.50×10 ⁻²	HOMO→LUMO(67)
	S ₀ →S ₂	400.52	3.09	5.00×10 ⁻⁴	HOMO→LUMO+2 (53)
	S ₀ →S ₃	388.86	3.19	8.00×10 ⁻²	HOMO-5→LUMO(64)
	S ₀ →S ₄	339.39	3.65	1.45×10 ⁻²	HOMO-8→LUMO(52)
	S ₀ →S ₅	338.21	3.66	3.71×10 ⁻²	HOMO-2→LUMO(39)
	S ₀ →S ₆	319.56	3.88	2.42×10 ⁻²	HOMO-1→LUMO(49)
P ₆	S ₀ →S ₁	526.77	2.35	2.69×10 ⁻¹	HOMO→LUMO(65)
	S ₀ →S ₂	490.58	2.53	5.90×10 ⁻³	HOMO-1→LUMO+1(64)
	S ₀ →S ₃	462.77	2.68	1.12×10 ⁻²	HOMO→LUMO+3 (55)
	S ₀ →S ₄	435.72	2.84	7.49×10 ⁻²	HOMO-1→LUMO(64)
	S ₀ →S ₅	385.01	3.22	1.00×10 ⁻⁴	HOMO-4→LUMO (59)
	S ₀ →S ₆	336.76	3.68	4.00×10 ⁻⁴	HOMO-8→LUMO(62)
P ₇	S ₀ →S ₁	520.27	2.38	3.06×10 ⁻¹	HOMO→LUMO(64)
	S ₀ →S ₂	499.83	2.48	1.38×10 ⁻²	HOMO-1→LUMO+1(48)
	S ₀ →S ₃	461.72	2.68	2.03×10 ⁻²	HOMO→LUMO+3 (56)
	S ₀ →S ₄	422.14	2.93	1.35×10 ⁻¹	HOMO-1→LUMO(65)
	S ₀ →S ₅	388.03	3.19	2.00×10 ⁻⁴	HOMO-5→LUMO(63)
	S ₀ →S ₆	336.09	3.69	5.00×10 ⁻⁴	HOMO-8→LUMO(58)
P ₈	S ₀ →S ₁	499.38	2.48	8.08×10 ⁻²	HOMO→LUMO+1 (40)
	S ₀ →S ₂	485.27	2.55	1.64×10 ⁻²	HOMO→LUMO(44)
	S ₀ →S ₃	446.36	2.77	2.85×10 ⁻¹	HOMO-2→LUMO(46)
	S ₀ →S ₄	418.62	2.96	3.26×10 ⁻²	HOMO-2→LUMO(49)
	S ₀ →S ₅	395.93	3.13	1.71×10 ⁻¹	HOMO-1→LUMO(59)
	S ₀ →S ₆	362.49	3.42	9.00×10 ⁻³	HOMO-5→LUMO(57)
P ₉	S ₀ →S ₁	490.34	2.53	4.90×10 ⁻³	HOMO→LUMO+2 (66)
	S ₀ →S ₂	430.60	2.88	2.63×10 ⁻¹	HOMO-1→LUMO(60)
	S ₀ →S ₃	420.78	2.94	7.40×10 ⁻³	HOMO-3→LUMO+1 (56)
	S ₀ →S ₄	412.47	3.01	1.62×10 ⁻¹	HOMO→LUMO+1 (51)
	S ₀ →S ₅	368.80	3.36	1.40×10 ⁻³	HOMO-7→LUMO+1 (56)
	S ₀ →S ₆	356.13	3.48	1.47×10 ⁻¹	HOMO-2→LUMO(55)
P ₁₀	S ₀ →S ₁	427.82	2.89	1.62×10 ⁻¹	HOMO-1→LUMO(60)
	S ₀ →S ₂	421.91	2.94	2.84×10 ⁻²	HOMO-3→LUMO+1(48)
	S ₀ →S ₃	400.73	3.09	6.59×10 ⁻²	HOMO→LUMO+1 (55)
	S ₀ →S ₄	369.29	3.35	5.00×10 ⁻⁴	HOMO-6→LUMO+1 (58)
	S ₀ →S ₅	355.22	3.49	9.65×10 ⁻²	HOMO-2→LUMO(63)
	S ₀ →S ₆	329.68	3.76	1.41×10 ⁻²	HOMO-1→LUMO+1(44)

2.4.3 Photovoltaic properties

The efficiency (η) of solar cell devices in converting sunlight into electricity depends on several crucial elements, including the incident solar power (P_{inc}), open-circuit photovoltage (V_{oc}), density of short-circuit current (J_{sc}), fill factor (FF). The efficiency, η , can be computed using Eq. (12)⁶¹:

$$\eta = \frac{J_{sc}V_{oc}FF}{P_{inc}} \quad (12)$$

The V_{oc} , which is a critical parameter for DSSC devices, can be expressed as the difference between E_{LUMO} of the dye and E_{CB} of TiO_2 , as described in Eq. (12). **Table 4** displays the predicted theoretical values of the V_{oc} for the examined dyes, which vary from 0.89 eV to 1.38 eV. The positive values suggest that transfer of electron from the examined substances P_i to TiO_2 will occur easily. Moreover, these values are adequate to achieve efficient injection of electron. Furthermore, these dyes may be employed as sensitizers due to the electron injection mechanism from the excited dye to the CB of TiO_2 .

Table 4 E_{HOMO} , E_{LUMO} and V_{oc} values of the investigated molecules achieved with B3LYP/6-31G (d, p) levels.

Dyes	E_{HOMO} (eV)	E_{LUMO} (eV)	V_{oc} (eV)
P₁	-5.01	-3.04	0.96
P₂	-5.28	-2.98	1.02
P₃	-4.94	-3.01	0.99
P₄	-5.01	-3.04	0.95
P₅	-5.23	-3.11	0.89
P₆	-4.83	-2.88	1.11
P₇	-4.82	-2.84	1.15
P₈	-4.88	-2.62	1.38
P₉	-5.02	-3.00	0.10
P₁₀	-5.38	-2.96	1.04
TiO₂(CB)	-7.16	-4.00	****

The current investigation reveals several essential characteristics in DSSCs, such as intramolecular charge transfer, E_{dye} , E_{dye}^* , and ΔG_{inject} toward the TiO_2 surface⁶². A comprehensive description of these factors is given in **Table 5**.

It should be noted that Koopman's theorem has been utilized to calculate the value of E_{dye} by taking the reciprocal of the E_{HOMO} value. Furthermore, the value of E_{dye}^* may be computed via Eq. (12).

Table 5. The oscillator strength maximum (f), ΔG_{inject} , light harvesting efficiency (LHE) and intra-molecular charge transfer energy of dyes computed using TD-DFT at B3LYP/6-31G(d,p) level of theory

Dyes	E_{dye}	E_{ex}	E_{dye}^*	ΔG_{inject}	f	LHE
P₁	5.01	2.47	2.54	-1.45	0.13	0.26
P₂	5.28	2.80	2.48	-1.52	0.24	0.43
P₃	4.94	2.36	2.57	-1.43	0.24	0.42
P₄	5.01	1.64	3.37	-0.62	0.10	0.21
P₅	5.23	2.56	2.67	-1.33	0.25	0.44
P₆	4.83	2.35	2.48	-1.52	0.27	0.46
P₇	4.82	2.38	2.44	-1.56	0.31	0.50
P₈	4.88	2.77	2.11	-1.89	0.28	0.48
P₉	5.02	2.88	2.14	-1.85	0.26	0.45
P₁₀	5.38	2.89	2.48	-1.51	0.16	0.31

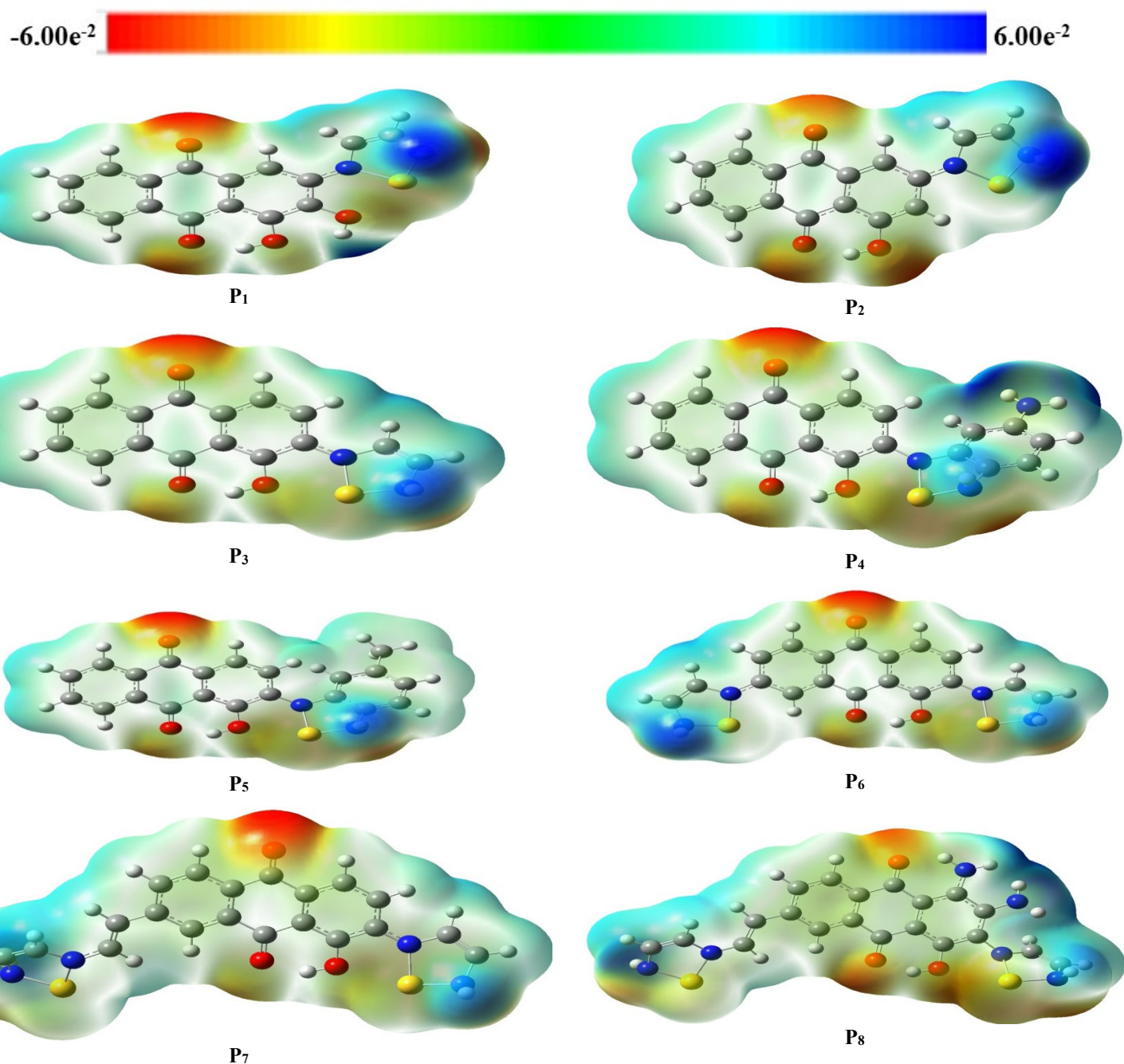
The E_{dye}^* values for the then dyes under study, as listed in **Table 5**, exhibited an ascending sequence as follows: **P₈ < P₉ < P₇ < P₂ < P₆ < P₁₀ < P₁ < P₃ < P₅ < P₄**. **P₈** has the highest level of oxidation among these dyes, while **P₄** demonstrates the lowest. It is important to emphasize that the ΔG_{inject} values for injection of electron from the excited state of the dye into the CB of TiO_2 were calculated using Eq. 11. A negative ΔG_{inject} value suggests that the electron injection process from the dye to the TiO_2 is spontaneous and can be performed without constraint for all sensitizers. The opposite of the ΔG_{inject} value follows the following sequence: **P₈ < P₉ < P₇ < P₂ < P₆ < P₁₀ < P₁ < P₃ < P₅ < P₄**. Consequently, the injection process will be relatively facile from **P₄** to the TiO_2 semi-conductor, and more difficult from **P₈** to the TiO_2 semi-conductor.

LHE, or Light Harvesting Efficiency, is the measure of how effectively a dye absorbs incident light. Thus, it is preferable for the LHE of dyes to be maximized in order to optimize the photocurrent response. **Table 5** presents the computed LHE values for the primary absorption peaks that exhibit the highest oscillation strength (f) for the dyes currently being used. These values range from approximately 0.21 to 0.50, with a slight increase observed with increasing oscillator strength. This implies that all sensitizers yield comparable photocurrent responses. On the other hand, the LHE parameter is

connected to the oscillator strength, as shown in Eq. (10), which is directly determined from TD-DFT computations. The data presented in Table 5 indicates that **P7** and **P8** exhibit a substantial oscillator strength, indicating that the most favorable π -conjugation system facilitates effective electron injection. Transitions with a notable oscillator strength were the ones taken into account. The findings indicate that all dyes possess the capacity to amplify the transformation of substantial quantities of sunlight into electrical energy when employed as the electron donor in DSSCs.

2.4.4 Molecular electrostatic potential

Molecular electrostatic potential (MEP) investigations examine the regions of positive and negative charge distribution in the investigated compounds, aiding in the anticipation of reactive sites. The molecular electrostatic potentials (MEPs) of the ten dyes under investigation, were calculated using the B3LYP/SDD/6-31+G(d,p) method. These MEPs are illustrated in Fig. 7. The MEP surfaces are color-coded to reflect the negative, positive, and neutral zones. The negative zone is shown by the color red, the positive zone by blue, and the neutral zone by green. The red-colored negative region is predominantly concentrated around the oxygen atoms in the ten dyes studied, suggesting that this specific location is vulnerable to electrophilic attack.



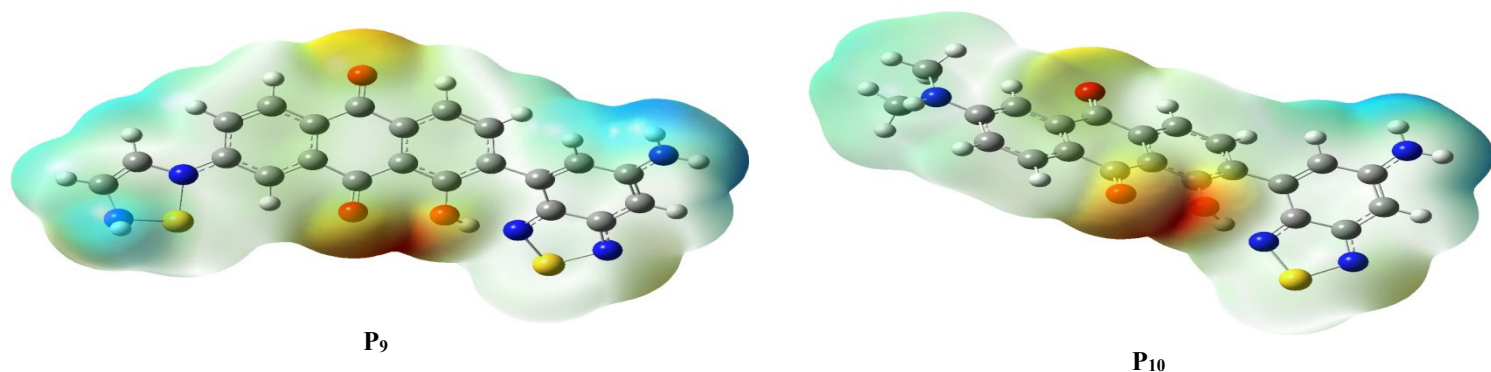


Fig. 7. Molecular electrostatic potential of the dyes studied, calculated using the B3LYP functional and 6-31G(d,p) base.

In contrast, the nitrogen, carbon, and hydrogen atoms are predominantly found in the positive region (shown by the blue color) of the **P1**, **P2**, **P3**, **P5** and **P6** dyes. This suggests that these locations have a high potential for nucleophilic attack. The remaining regions of the molecule are neutral, without any electrostatic potential.

The MEP map employs a range of colors to indicate electron concentrations, with electron density values ($V(r)$) ascending in the following sequence: Red > Yellow > Green > Blue. Furthermore, the MEP is most suitable for identifying locations for both intra- and intermolecular interactions.

3. Conclusions

This paper provides a comprehensive theoretical analysis of the geometric, electronic, optical, and photovoltaic properties of ten dyes using DFT/TD-DFT. The findings reveal that modifications in the chemical structures can significantly optimize these properties. Specifically, the B3LYP functional was identified as the best choice for predicting the geometric and electronic features of the dyes. TD-DFT with the B3LYP-6-31G(d,p) basis set effectively analyzed the absorption properties, with absorption wavelengths spanning from 427.82 nm to 755.93 nm and characterized by delocalized π - π^* transitions across all ten dyes in the UV/Vis spectrum. The calculated band gaps for the dyes ranged from 1.93 eV to 2.42 eV, with a decreasing trend in the following order: **P10** > **P2** > **P8** > **P5** > **P9** > **P7** > **P1** > **P4** > **P6** > **P3**. This clearly indicates that increased conjugation leads to a reduction in the band gap. Furthermore, the V_{oc} values for TiO_2 , ranging from 0.89 eV to 1.38 eV, suggest good potential for efficient electron injection. Overall, these dyes show significant promise for use in DSSCs, and the computational methods presented here provide a valuable tool for predicting the electronic, optical, and photovoltaic properties of other materials, supporting the design of new compounds for DSSC applications.

Availability of data and material

All data generated or analyzed during this study are included in this published article.

References

1. Teymourinia H., Salavati-Niasari M., Amiri O., and Farangi M. (2018) Facile synthesis of graphene quantum dots from corn powder and their application as down conversion effect in quantum dot-dye-sensitized solar cell. *J. Mol Liq.*, 251, 267–272.
2. Muñoz-García AB., Benesperi I., Boschloo G., Concepcion JJ., Delcamp JH., Gibson EA., Freitag M., and Anders F. (2021) Dye-sensitized solar cells strike back. *Chem Soc Rev.*, 50, 12450-12550.
3. Ajel MK., and Al-nayili A. (2023) Synthesis, characterization of Ag-WO₃/bentonite nanocomposites and their application in photocatalytic degradation of humic acid in water. *En Sci Pollut Res.*, 30, 20775–20789.
4. Cole JM., Pepe G., Al Bahri OK., and Cooper CB. (2019) Cosensitization in Dye-Sensitized Solar Cells. *Chem Rev.*, 119, 7279–7327.
5. Bandara TMWJ., Hansadi JMC., and Bella F. (2022) A review of textile dye-sensitized solar cells for wearable electronics. *Ionics (Kiel)*, 28, 2563–2583.
6. Al-abidy M., and Al-nayili A. (2023) Enhancement of photocatalytic activities of ZnFe₂O₄ composite by incorporating halloysite nanotubes for effective elimination of aqueous organic pollutants. *Env Monit Assess.*, 195, 1–15.
7. Aboulouard A., Gultekin B., Can M., Erol M., Jouaiti A., Elhadadi B., Ceylan Z., and Serafettin D. (2020) Dye sensitized solar cells based on titanium dioxide nanoparticles synthesized by flame spray pyrolysis and hydrothermal sol-gel methods: a comparative study on photovoltaic performances. *J Mater Res Technol.*, 9, 1569–1577.
8. Irfan M., Khan MI., Amami M., Ahson R., and Alabbad EA. (2022) Effect of Fe ions beam on the structural, optical, photovoltaic properties of TiO₂ based dye-sensitized solar cells. *Opt Mater.*, 123, 111794.
9. Albdiry M., and Al-Nayili A. (2023) Ternary sulfonated graphene/polyaniline/carbon nanotubes nanocomposites for high performance of supercapacitor electrodes. *Polym Bull.*, 80, 8245–8258.
10. Aboulouard A. (2022) Effect of Temperature and Electrode Thickness on the Performance of Dye-Sensitized Solar Cells. *Phys Chem Res.*, 10, 23–30.
11. Gao N., Huang L., Li T., Song J., Hu H., Liu Y., and Ramakrishna S. (2020) Application of carbon dots in dye-sensitized

- solar cells: A review. *J Appl Polym Sci.*, 137, 48443.
12. Al-nayili A., and Rzoqy M. (2022) Local silica sand as a silica source in the synthesis of Y zeolite. *Asia-Pacific J Chem Eng.*, 17, e2824.
 13. Selvaraj B., Shanmugam G., Kamaraj S., Thirugnanasambandam E., Peters S., Gunasekeran A., Anandan S., and Pillai RS. (2022) Effect of Copper and Cobalt Metal Complex Redox Mediator Based Xanthan Gum Gel Electrolyte Materials on Performance of Dye Sensitized Solar Cells. *CheSel.*, 7, e202203197.
 14. Karthick SN., Hemalatha KV., Balasingam SK., Manik Clinton F., Akshaya S., and Kim HJ. (2019) Dye-Sensitized Solar Cells: History, Components, Configuration, and Working Principle. *Int Eng Funct Mater Dye Sol Cells.*, 1–16.
 15. Al-Nayili A., and Albdiry M. (2021) Identification of active structure and catalytic efficiency of MCM-22 zeolite detemplated by two different processes. *J Porous Mater.*, 28, 1439–1448.
 16. Passantino JM., Wolfe KD., Simon KT., Cliffel DE., and Jennings GK. (2020) Photosystem I Enhances the Efficiency of a Natural, Gel-Based Dye-Sensitized Solar Cell. *ACS Appl Bio Mater.*, 3, 4465–4473.
 17. Elghazali A., Aboulouard A., Zouitina S., Tounsi A., and El idrissi M. (2023) First-Principles Study on Optoelectronic and Photovoltaic Properties in a P3HT/PCBM Complex. *Phys Chem Res.*, 11, 299–313.
 18. Kim J-H., Kim D-H., So J-H., and Koo H. J. (2022) Toward Eco-Friendly Dye-Sensitized Solar Cells (DSSCs): Natural Dyes and Aqueous Electrolytes. *Energies* 15.
 19. Amogne NY., Ayele DW., and Tsigie YA. (2020) Recent advances in anthocyanin dyes extracted from plants for dye sensitized solar cell. *Mater Renew Sustain Energy.*, 9, 23.
 20. Ruess R., Scarabino S., Ringleb A., Nonomura K., Vlachopoulos N., Hagfeldt A., Gunther W., and Schlettwein D. (2019) Diverging surface reactions at TiO₂- or ZnO-based photoanodes in dye-sensitized solar cells. *Phys Chem Chem Phys.*, 21, 13047–13057.
 21. Alwan SH., Salem KH., and Alshamsi HA. (2022) Visible light-driven photocatalytic degradation of Rhodamine B dye onto TiO₂/rGO nanocomposites. *Mater Today Commun.*, 33, 104558.
 22. Abdulhusain ZH., Alshamsi HA., and Salavati-Niasari M. (2022) Silver and zinc oxide decorated on reduced graphene oxide: Simple synthesis of a ternary heterojunction nanocomposite as an effective visible-active photocatalyst. *Int J Hydrogen Energy.*, 47, 34036–34047.
 23. Manafi P., Nazoockdast H., Karimi M., Sadighi M., and Magagnin L. (2021) A study on the microstructural development of gel polymer electrolytes and different imidazolium-based ionic liquids for dye-sensitized solar cells. *J. Power Sources.*, 481, 228622.
 24. Mohamad A. A. (2019) Physical properties of quasi-solid-state polymer electrolytes for dye-sensitized solar cells: A characterisation review. *Sol Energy.*, 190, 434–452.
 25. Gbair GA., and Alshamsi H. A. (2022) Facile green synthesis of CuO-ZnO nanocomposites from *Argyrea nervosa* leaves extract for photocatalytic degradation of Rhodamine B dye. *Biomass Convers Biorefinery.*, 14, 28117–28132.
 26. Pawar M., Sendogdular ST., and Gouma P. (2018) A Brief Overview of TiO₂ Photocatalyst for Organic Dye Remediation: Case Study of Reaction Mechanisms Involved in Ce-TiO₂ Photocatalysts System. *J. Nanomater.*, 2018, 5953609.
 27. Wang D., Luo H., Liu L., Wei W., and Li L. (2019) Adsorption characteristics and degradation mechanism of metronidazole on the surface of photocatalyst TiO₂: A theoretical study. *Appl Surf Sci.*, 478, 896–905.
 28. Gao Q., Si F., Fang Y., Chen X., and Zhang S. (2019) Hydrogenated F-doped TiO₂ for photocatalytic hydrogen evolution and pollutant degradation. *Int J Hydrogen Energy* 44, 8011–8019.
 29. Bharatvaj J., Preethi V., and Kanmani S. (2018) Hydrogen production from sulphide wastewater using Ce³⁺-TiO₂ photocatalysis. *Int J Hydrogen Energy.*, 43, 3935–3945.
 30. Diany R., Kerraj S., Aboulouard A., Syed A., Zeroual A., Bahkali A H., El idrissi M., Salah M., and Tounsi A. (2024) Enhancing dye sensitized solar cells performance through quinoxaline based organic dye sensitizers. *Journal of Computational Electronics.*, 1-14.
 31. Senthil Kumar R., and Gnanavel B. (2017) High performance catalytic activity of pure and silver (Ag) doped TiO₂ nanoparticles by a novel microwave irradiation technique. *J. Mater Sci Mater Electron.*, 28, 4253–4259.
 32. Ma R., Wang X., Huang J., Song J., Zhang J., and Wang X. (2017) Photocatalytic degradation of salicylic acid with magnetic activated carbon-supported F-N codoped TiO₂ under visible light. *Vacuum.*, 141, 157–165.
 33. Rased N.H., Vengadaesvaran B., Raihan S.R.S., and Rahim N. A. (2021) Introduction to solar energy and its conversion into electrical energy by using dye-sensitized solar cells. *En. Mater Fundam to Appl.*, 139–178.
 34. Albo Hay Allah M. A., and Alshamsi H. A. (2022) Green synthesis of ZnO NPs using *Pontederia crassipes* leaf extract: characterization, their adsorption behavior and anti-cancer property. *Biomass Convers Biorefinery.*, 14(9), 10487–10500.
 35. Jeyaraman AR., Balasingam S K., Lee C., Lee H., Balakrishnan B., Manickam S., Yougseak J., and Kuzhandaivel H. (2019) Enhanced solar to electrical energy conversion of titania nanoparticles and nanotubes-based combined photoanodes for dye-sensitized solar cells. *Mater Lett.*, 243, 180–182.
 36. Karami M., Ghanbari M., Alshamsi H.A., Ghiyasiyan-Arani M., and Salavati-Niasari M. (2021) The effect of Cu–PbI₂ nanocomposite fabricated by the sonochemical route on electrochemical hydrogen storage characteristics. *Int. J. Hydrogen Energy.*, 46, 19074–19084.
 37. Zouitina S., Aboulouard A., Ghazali A., Tounsi A., and El idrissi M. (2023) Computational Study of New Small Molecules based Thiophene as Donor Materials for Bulk Heterojunction Photovoltaic Cells. *J. Fluoresc.*, 33, 553–563.
 38. Fonseca Guerra C., Snijders J.G., Te Velde G., and Baerends E. J. (1998) Towards an order-N DFT method. *Theor Chem Acc.*, 99, 391–403.
 39. Laurent A.D., and Jacquemin D. (2013) TD-DFT benchmarks: A review. *Int. J. Quantum Chem.*, 113, 2019–2039.
 40. Becke AD. (1993) Density-functional thermochemistry. III. The role of exact exchange. *J Chem Phys.*, 98, 5648–5652.
 41. Shafiq I., Wu G., Khan M., Khan M.U., Alshehri S. M., and Chen K. (2024) Exploration of promising photovoltaic properties

- of bisoindigo-based heterocyclic chromophores for organic solar cells: A DFT/TD-DFT study. *J. Saud. Chem. Soc.*, **28**, 101878.
42. Latif W., Hanan M., Jaffar A., Shafique A., Aziz S., Kamran K., and Mahr M. S. (2025). SFX-based hole transport materials for advancement in perovskite and organic solar cells: DFT computational insights and photovoltaic improvements. *Mat. Sci. Eng.: B.*, 313, 117974.
 43. Hadi H., and Alshehri, S. (2025) A leap forward in the optimization of organic solar cells: DFT-based insights into the design of NDI-based donor-acceptor-donor structures. *Mat. Sci. Semiconductor Process.*, **185**, 108994.
 44. Clark T., Chandrasekhar J., Spitznagel G. W., and Schleyer P.V. R. (1983) Efficient diffuse function-augmented basis sets for anion calculations. III. The 3-21+G basis set for first-row elements, Li-F. *J. Comput Chem.*, **4**(3), 294–301.
 45. Radom L., Hehre W.J., Pople J.A. (1971) Molecular Orbital Theory of the Electronic Structure of Organic Compounds. VII. A Systematic Study of Energies, Conformations, and Bond Interactions. *J. Am. Chem. Soc.*, **93**, 289–300.
 46. Hariharan P.C., and Pople J. A. (1973) The influence of polarization functions on molecular orbital hydrogenation energies. *Theor Chim Acta.*, **28**, 213–222.
 47. Hehre W.J., Ditchfield R., and Pople J. A. (1972) Self-Consistent Molecular Orbital Methods. XII. Further Extensions of Gaussian-Type Basis Sets for Use in Molecular Orbital Studies of Organic Molecules. *J. Chem Phys.*, **56**, 2257–2261.
 48. Kim Y-S., Kim S-H., Kim T-K., and Son Y-A. (2008) Characteristics of HOMO and LUMO potentials by altering substituents: computational and electrochemical determination. *Text Color Finish.*, **20**, 41–46.
 49. Gallmetzer J.M., Kröll S., Daniel W., Dominik W., Mihai I-V., Engelbert P., Niyasi S.S., and Werner D. (2022) Anthraquinone and its derivatives as sustainable materials for electrochemical applications – a joint experimental and theoretical investigation of the redox potential in solution. *Phys Chem Chem Phys.*, **24**, 16207–16219.
 50. Tandon H., Chakraborty T., and Suhag V. (2020) A fundamental approach to compute atomic electrophilicity index. *J Math Chem.*, **58**, 2188.
 51. Zhou Z., and Parr R.G. (1989) New Measures of Aromaticity: Absolute Hardness and Relative Hardness. *J. Am. Chem. Soc.*, **111**, 7371–7379.
 52. Parr R.G., Szentpaly L.V., and Liu S. (1999) Electrophilicity Index, *J. Am. Chem. Soc.*, **121**, 1922-1924.
 53. Stokes E.D., and Chu T.L. (1977) Diffusion lengths in solar cells from short-circuit current measurements. *Appl Phys Lett.*, **30**, 425–426.
 54. Zhang Z.L., Zou L.Y., Ren A.M., Liu Y.F., Feng J.K., and Sun C.C. (2013) Theoretical studies on the electronic structures and optical properties of star-shaped triazatruxene/heterofluorene co-polymers. *Dye Pigment.*, **96**, 349–363.
 55. Shabbir S., Shaari A., Haq B.U., Ahmed R., AlFaify S., Ahmed M., and Laref A. (2021) First-principles investigations of electronic structures and optical spectra of wurtzite and sphalerite types of ZnO_{1-x}S_x (x=0, 0.25, 0.50, 0.75 & 1) alloys. *Mater Sci Semicond Process.*, **121**, 105326.
 56. Divya V V., and Suresh C.H. (2020) Density functional theory study on the donating strength of donor systems in dye-sensitized solar cells. *New J. Chem.*, **44**, 7200–7209.
 57. Kerraj S., Salah M., Chtita S., El idrissi M., Belaaouad S., Moutaabd M., Nivedita A., and Komiha N. (2022) Theoretical study of photovoltaic performances of Ru, Rh and Ir half sandwich complexes containing N,N chelating ligands in Dye-Sensitized Solar Cells (DSSCs). DFT and TD-DFT investigation. *Comput Theor Chem.*, **1209**, 113630.
 58. Tandon H., Chakraborty T., and Suhag V. (2020) A scale of atomic electronegativity in terms of atomic nucleophilicity index. *Found Chem.*, **22**, 335–346.
 59. Hosseinezhad M., Movahedi J., and Nasiri S. (2020) High stability photosensitizers for dye-sensitized solar cells: Synthesis, characterization and optical performance. *Opt Mater.*, **109**, 110198.
 60. Liu S., Yuan J., Deng W., Luo M., Xie Y., Liang Q., Yingping Z., Zhicai H., Hogbin W., and Cao Y. (2020) High-efficiency organic solar cells with low non-radiative recombination loss and low energetic disorder. *Nat Photonics.*, **14**, 300–305.
 61. Guo Z., Liang W.Z., Zhao Y., and Chen G. (2008) Real-time propagation of the reduced one-electron density matrix in atom-centered orbitals: Application to electron injection dynamics in dye-sensitized TiO₂ clusters. *J. Phys Chem C.*, **112**, 16655–16662.
 62. Tian H., Yang X., Cong J., Chen R., Teng C., Liu J., Yan H., Lei W., and Sun L. (2010) Effect of different electron donating groups on the performance of dye-sensitized solar cells. *Dye Pigment.*, **84**, 62–68.

